Physically Based Simulation and Rendering of Urban Thermography

José Pedro Aguerre,[1] Elena García-Nevado,[2] Jairo Acuña Paz y Miño,[2] Eduardo Fernández[1] and Benoit Beckers[2]

[1]Universidad de la República, Uruguay
{jpaguerre, eduardof}@fing.edu.uy
[2]Université de Pau et des Pays de l'Adour, France
{e.garcia-nevado, j.acuna, benoit.beckers}@univ-pau.fr

Abstract
Urban thermography is a non-invasive measurement technique commonly used for building diagnosis and energy efficiency evaluation. The physical interpretation of thermal images is a challenging task because they do not necessarily depict the real temperature of the surfaces, but one estimated from the measured incoming radiation. In this sense, the computational rendering of a thermal image can be useful to understand the results captured in a measurement campaign. The computer graphics community has proposed techniques for light rendering that are used for its thermal counterpart. In this work, a physically based simulation methodology based on a combination of the finite element method (FEM) and ray tracing is presented. The proposed methods were tested using a highly detailed urban geometry. Directional emissivity models, glossy reflectivity functions and importance sampling were used to render thermal images. The simulation results were compared with a set of measured thermograms, showing good agreement between them.

Keywords: physically based modelling, modelling, ray tracing, rendering, numerical analysis, methods and applications

ACM CCS: • Computing methodologies → Rendering; Ray tracing; Modelling methodologies; • Applied computing → Architecture (buildings)

1. Introduction

Just as digital photographic cameras capture incoming light radiation and transform it into colours, thermal cameras capture incoming thermal radiation and transform it into temperatures [VM17]. In a real-world environment, light is typically emitted by few surfaces (the Sun or artificial sources such as a lamp) and reflected by the rest of the scene. Thermal radiation, on the other hand, is emitted by every surface at a temperature above the absolute zero, and it is also reflected by the objects. Hence, in this part of the spectrum, the urban surfaces become radiation sources. Thermograms display an estimated temperature of the surfaces that is derived from the combined emitted and reflected radiation arriving at the lens.

Thermography is widely used in many industries and scientific areas. Civil engineers and architects use thermal cameras for building diagnostics and energy efficiency evaluation [EGGA18]. Thermal imaging of urban scenes has become a recent topic of interest because it provides spatialized information about the thermal behaviour of the city [BGN19]. However, the interpretation of the resulting images is a difficult task [DICM05], and therefore numer-

ical simulations have been developed for assessing the reliability of measurements [PMMR*06, ANGN*19]. Moreover, combining thermal images and simulations can help understanding the physical, material and geometrical complexity that is involved in urban environments.

The computational simulation of photography has long been subject of study for both physics and computer graphics communities [War94]. Material properties such as reflectivity, transparency and absorptivity in the visible spectrum have been widely researched, looking for more realistic simulation conditions in physically based rendering [PJH16]. Nevertheless, its thermal counterpart, namely, *thermography simulation*, has not been addressed with the same intensity, although it is gaining attention in the graphics community [HB18, MBP18, KBBH19].

Thermography has been used for comparison and validation of thermal simulations. Hénon *et al.* [HMLV12] used the SOLENE-microclimat model to perform thermal simulations of a set of buildings. The results were compared with temperature measurements obtained from an airborne thermal camera, showing differences of
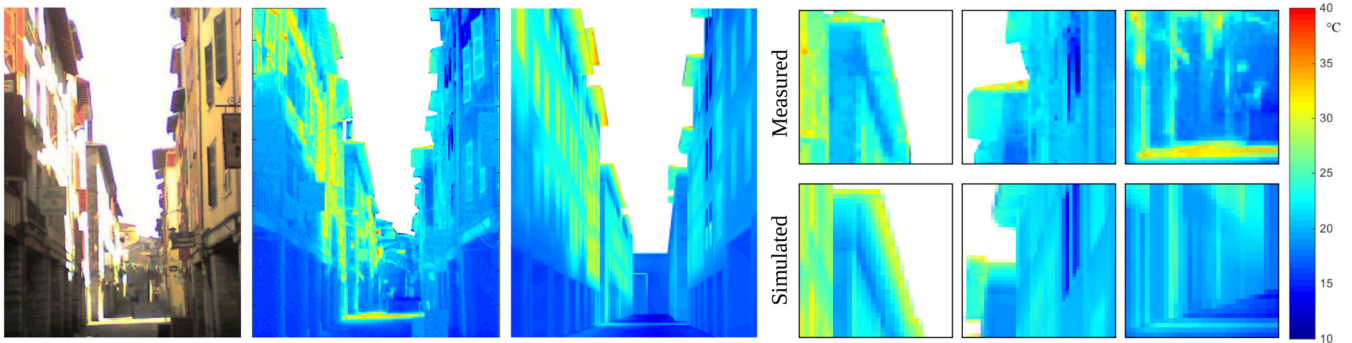
Figure 1: *Urban scene of Tonneliers street in Bayonne, France. From left to right: photography in a perspective view of the street, measured thermogram of the scene, rendered thermogram using the proposed methodology and different quadrants showing the details of the results. All the images were built over the same colour map.*

around 2 to 5 °C in the generated images. This bias was attributed to the geometric and material simplifications made in the 3D model. Rodler *et al.* [RGMB18] presented a computational model based on the finite difference method to analyse the thermal behaviour of a building and its environment. The results were compared with measured thermograms and contact temperature sensors, obtaining some uncertainties related to the adopted simplifications in the building energy model.

Aguerre *et al.* [ANGN*19] showed that finite element method (FEM) is a suitable tool for urban thermography simulation. The simulation results were compared to infrared images, obtaining differences of up to 5 °C. This paper is the next step of this research. It is of particular interest to analyse the integration of high level of detail geometries [NGDA*16] and its impact on the computational performance. Furthermore, for thermography rendering, working with suitable infrared material characteristics such as directional emissivities and reflectivity functions [SW98] and their effect on the results must be studied. In this sense, the main contributions of the present work, in comparison with [ANGN*19], are the integration of directional infrared properties in the simulations, the addition of a rendering stage in which these models are especially important and the use of a much detailed urban geometry to obtain a better matching between measured and rendered results.

To accomplish these purposes, an assessment of the impact of the integration of directional infrared material properties for urban thermography simulation is developed. A physically based simulation methodology built on a combination of the FEM code Cast3m [CDP11] and the ray tracing kernel Embree [WWB*14] is presented for infrared rendering. The simulated thermograms were compared to the results of a measurement campaign performed in the city of Bayonne, France, where a sequence of thermal images was captured throughout a clear sky day [GN19]. A directional emissivity model was estimated from thermographic observations, and a glossy reflectivity function was used in the simulations to account for infrared radiation reflections. Compared with measurements, the methodology exhibits accurate precision and good computational performance. The source code used for infrared rendering is freely available for anyone to inspect and alter [Agu20].

2. Long-Wave Modelling and Simulation

Every body at a temperature above the absolute zero emits and absorbs radiation. Radiation is energy in the form of electromagnetic waves that is propagated through vacuum or material mediums at the speed of light. The spectral distribution (wavelength) of the radiation emitted by a black body depends solely on its temperature (Planck's law). A black body can be defined as an ideal body that absorbs all of the incident radiation no matter the direction and, to stay in thermal equilibrium, emits radiation at the same ratio (as a Lambertian emitter). Integrating over the whole spectrum, Stefan's law describes the total radiative density flux of the black body as [HMS15]:

$$\Phi^{black}(T) = \sigma T^4, \qquad (1)$$

where σ is the Stefan–Boltzmann constant ($\approx 5.67 \times 10^{-8}$ W m^{-2} K^{-4}) and T the black body temperature.

Urban surfaces cannot always be assumed as black bodies because of the wide variety of materials used in construction. The notion of grey body is defined as a body whose spectral emissivity and absorptivity properties are independent of wavelength [Mod03]. A grey body emits a fraction of the total radiation emitted by the black body. This fraction (a number between 0 and 1) is called the emissivity ε. The total density of the grey body radiative flux is [HMS15]

$$\Phi^{grey}(T) = \varepsilon \sigma T^4. \qquad (2)$$

The emissivity depends on several factors, such as radiation wavelength, material roughness, geometrical imperfections and incidence angles. Regarding the emissivity wavelength dependence, a common assumption in studies involving solar radiation is to consider two well-defined regions: short (under 4 μm) and long (above 4 μm) spectra. In this case, materials are often called *semi-grey* [HMS15], and they are approximated using two different sets of properties that are uniform within each region. This assumption is used in the present work for urban elements.

Two kinds of ideal directional emissivity models are described in the literature for non-conductive materials in the thermal spectrum: very rough materials can be approximated with a perfectly diffuse
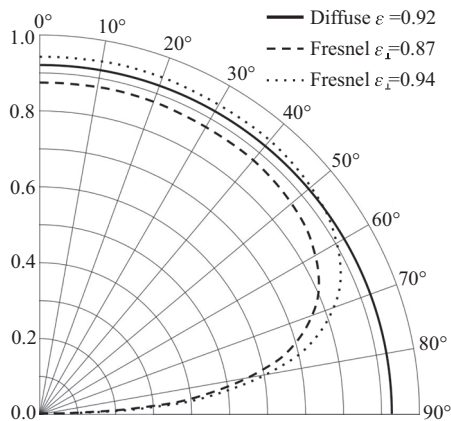
Figure 2: *Ideal directional emissivity models using Fresnel equations in the case of smooth surfaces (with $\varepsilon_\perp$ the normal emissivity of the material) and perfectly diffuse approximations for very rough surfaces.*

emission model, which implies a unique emissivity value for every direction. On the other hand, optically smooth surfaces such as glass are usually modelled using Fresnel's relations (following Schlick's approximation from the normal emissivity $\varepsilon_\perp$ [Sch94]), where the emissivity reaches its maximum value near the normal direction and shows smaller values for larger angles of incidence. Figure 2 shows examples of ideal models. A common assumption is that the emissivity values depend only on the zenith angle of view, that is, it has the same behaviour for different directions in the azimuthal angle.

Kirchhoff's law of thermal radiation states that the emissivity ε and the absorptivity α of any body in thermodynamic equilibrium are the same. For a grey, diffuse and opaque (i.e. without transmission) body, it can be stated that [HMS15]:

$$\varepsilon = \alpha = 1 - \rho, \tag{3}$$

where ρ is the reflectivity of the material. Kirchhoff's law is also true *directionally*: the directional emissivity is equal to the directional absorptivity for all directions.

The reflective properties of materials depend greatly on the wavelength of study. In the long-wave spectrum, surfaces tend to behave more specularly than in the visible spectrum. Perfectly smooth materials that follow Fresnel's emissivity model are completely specular reflectors, while diffuse emitters can present different reflectivity patterns, depending on their surface roughness. Construction materials such as concrete, mortar or wood are usually not smooth, making it necessary to study the emissivity and reflectivity models that approximate their behaviour.

Current scientific knowledge on the behaviour of materials in the infrared spectrum is limited. Directional emissivity and reflectivity in the long-wave spectrum are still a matter of study for experimental physics [PRS16]. Literature provides little information about these properties for construction materials [VM17] and tests to determine them are complex to perform outside a lab environment.

Long-wave radiation simulation is not as widely studied as its short-wave counterpart. This fact is partly explained by the differences between these two phenomena. On the one hand, the balance of thermal radiation at a point implies a self-dependence, because the incoming radiative flux depends on the temperature of the point, and vice versa [HMS15]. On the other hand, infrared radiation is emitted by every surface in the city, which brings the question of how to model the behaviour of multiple emitters and their energy exchange. The self-dependence issue is usually tackled by linearizing the flux and using last timestep temperatures to compute the current timestep radiation, treating it as an imposed flux [EDC14]. This approach does not ensure flux equilibrium because the temperatures can differ greatly between the previous and current timesteps. Using short timesteps helps reducing radiative flux differences but implies an increment in the computational costs. The radiation exchange between multiple emitters is commonly solved using sky view factor (SVF)-based approaches, which assume a uniform temperature of the urban context and an isotropic temperature distribution of the sky.

A second level of complexity for long-wave exchange simulations consists of accounting for the diffuse exchanges between the elements of the scene. In this context, radiosity becomes the most used technique for computing long-wave radiation in FEM systems (e.g. COMSOL multiphysics [COM18], ANSYS [SNY18] and Cast3m [CDP11])).

The integration of more complex graphical methods [THC*19] is necessary for modelling the optical properties of materials, to obtain greater detail in infrared radiation simulations [Mod03]. In thermal calculations where radiation has a greater significance, such as temperature calculations of satellite-like structures, considering the infrared optical properties can be important [vE13]. In thermography rendering, the integration of directional emissivities and reflectivities is necessary under some circumstances [HB18], especially when perspective views of the scene are captured [GN19].

Directional infrared properties (emissivity and reflectivity) have been used in previous works. Van Eekelen [vE13] presented an FEM approach to simulate satellite surface temperature considering non-grey surfaces and specular reflections. By using different simulation configurations, the author showed that the thermo-optical properties of the surfaces are an important tool for the thermal control of a satellite. Snyder *et al.* [SWZF97, SW98] and Li *et al.* [LSF99] introduced a variety of bidirectional reflectance distribution function (BRDF) models for studying land surface temperatures. Li *et al.* [LBM*09] performed a set of ray-tracing simulations of the thermal response of a cup for mid-wavelength infrared (1.3–3 μm) using a simplified global illumination model to consider reflections. Military studies are particularly interested in rendering mid-wave and long-wave radiation of fields for motion-detection; hence some approaches were presented using ray-tracing and empirical BRDF models [LCDG07, KSB*08]. Wu *et al.* [WZCH15] proposed a mid-wavelength BRDF and compared it with a thermal image of a set of buildings. Lagouarde *et al.* [LHK*10] modelled the directional anisotropy of a large-scale city centre based on airborne acquisition. To this day, no work has addressed the directional properties of long-wave radiation in a simulation with a detailed urban geometry as it was performed in the present study.
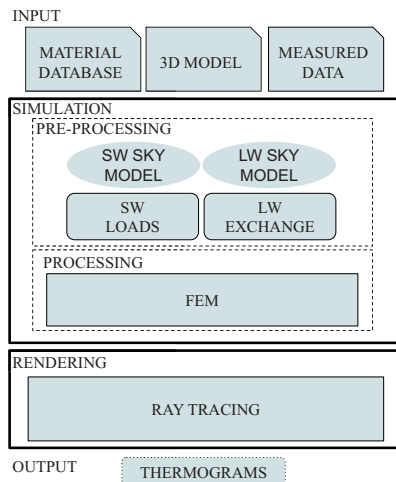
Figure 3: *Scheme of the computational model.*

Figure 4: *Diagram of heat transfer at the urban scale.*

3. Methods

This section presents a methodology to simulate urban surface temperatures and to render thermal images. This methodology starts from a set of inputs that are necessary to model reality. The 3D model of the scene and its associated material properties are used in all the stages of the simulation. *In situ* measurements or alternative physically based models are needed to estimate boundary conditions accurately. For example, short-wave horizontal irradiances and air temperatures must be measured or estimated because the system is strongly dependent on them.

The simulation process can be divided into two main steps (Figure 3). It includes a pre-processing stage where computations that are independent of temperature values are carried out, such as the calculation of short-wave loads and long-wave view factors. The processing stage uses the previous results to compute surface temperatures. Finally, a rendering post-processing stage is necessary to obtain the infrared thermograms.

3.1. Simulation

The temperature of a body is an expression of its energetic state, which is the result of its energy balance. The urban energy balance problem can be formulated as a conduction-dominant transient problem, where the conductivity properties of the scene greatly influence its thermal behaviour through time. Nevertheless, several boundary conditions must be considered in an urban study, which complicates the analysis and the involved computational methods [MGG*10, GDAB*17]. The transient energy balance is described using Fourier's law of heat conduction [LNS04]:

$$\rho_m c_p \frac{\partial T}{\partial t} = k \Delta T \quad \text{subject to:} \quad T = T_b \text{ on } \Gamma_b,$$

$$\text{and } -k \frac{\partial T}{\partial n} + q_s + h(T - T_{air}) + \varepsilon \sigma (T^4 - T_{env}^4) = 0 \text{ on } \Gamma_q. \quad (4)$$

This equation is a non-linear second-order partial differential equation. The first part represents heat conduction, while the subse-
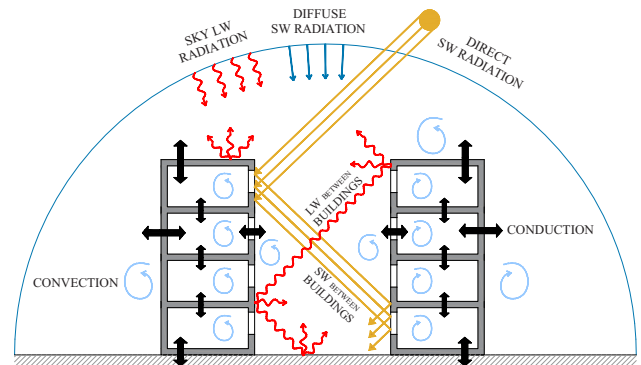
quent terms account for boundary conditions. Dirichlet conditions are imposed temperatures T_b in the interface Γ_b. Neumann conditions are imposed fluxes in Γ_q, in the form of absorbed short-wave radiation q_s (W m^{-2}), long-wave radiative exchange and convective heat transfer exchanged with the air. The vector n denotes the outward normal to the boundary Γ_q. T is the temperature of the surface in K, t represents time, while Δ is the Laplace operator. ρ_m (kg m^{-3}), c_p (J kg^{-1} K^{-1}) and k (W m^{-1} K^{-1}) are the mass density, specific heat and conductivity of the material. h is the convective heat transfer coefficient in W m^{-1} K^{-1}, and T_{air} is the air temperature. ε is the emissivity of the material and T_{env} is the average temperature of the environment. An initial temperature T_0 at $t = 0.0$s is necessary for solving this differential equation. The urban heat transfer problem is diagrammed in Figure 4.

Following Aguerre *et al.* [ANGN*19], we propose using FEM to address the processing stage, because it allows for the simulation of urban geometries using different types and sizes of elements, and because the results provide the temperature distribution across every surface based on the selected shape functions. This stage requires the heaviest computations because several physical phenomena must be incorporated in the calculations. The involved boundary fluxes (Neumann boundary conditions) are convection, short-wave radiation and long-wave radiation. Imposed temperatures (Dirichlet boundary conditions) are used to fix the ground temperature at a given depth.

The first task of the pre-processing stage is to estimate the short-wave loads at the urban surfaces. For this, two steps are necessary: the estimation of the sky emitted light and the calculation of the radiative exchange between the city objects. As proposed in [ANGN*19], the Liu and Jordan clear sky model [LJ60] is used to estimate the direct and diffuse sky emissions, taking the measured global horizontal irradiances as input. A sky vault partition [BB14] with 2400 tiles is used to account for the anisotropy of the emission. The radiance value for each tile is calculated with Perez all-weather sky model [PSM93]. After the sky emission is estimated, the radiosity method is used to compute the radiative exchange, which is a well-suited algorithm for dealing with urban environments composed of mainly diffuse surfaces in the short-wave spectrum. Extended form factors [SP89] are used to enable other kinds of reflections, such as the behaviour of window glasses (specular surfaces). This approach provides short computational times and negligible
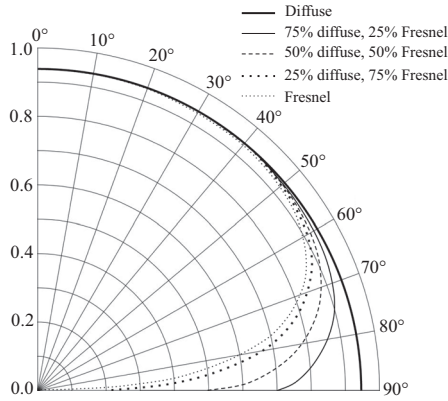
Figure 5: *Directional emissivity interpolated from two ideal models.*

error when compared to classical ray-based approaches, as shown in [AFB18]. The absorbed short-wave fluxes are then considered as the nodal imposed flux q_s by averaging the values of all the adjacent elements of each node.

3.1.1. *Long-wave radiation*

A typical approach followed by FEM systems is to integrate long-wave radiation in a similar way than convection, but using an iterative solver for dealing with the non-linearities and self-dependences associated with long-wave exchanges. The correspondent h coefficient, namely, h_{rad}, is recalculated several times for each timestep based on the emissivities and surrounding temperatures of each element. Most of the FEM packages work in this way, assuming grey-diffuse materials and using the radiosity algorithm for solving the exchange process [Cou06].

Typical construction materials are not perfect diffuse emitters/reflectors, which means that they emit and reflect different amounts of energy depending on the angle of incidence. Handling the directional properties (i.e. non-diffuse properties) of infrared radiation may not pose a significant impact on the temperature results, but it becomes important when capturing the infrared response of a scene with a thermal camera. Hence, to maintain consistency in the methodology, we propose accounting for the directionality of long-wave radiation across all the stages of the simulation, although the focus is on analysing the results in the thermography rendering stage instead of in the FEM raw temperature results.

A linear combination of the ideal emissivity models presented in Figure 2 (Fresnel and diffuse) is used to account for non-diffuse materials, where greater surface roughness implies greater contribution of the diffuse part (Figure 5). Smooth construction materials like glass are modelled with values closer to the Fresnel model and very specular reflectivities. Rough surfaces, such as wood or stone, follow a more diffuse emission pattern and a glossy reflectivity behaviour, which is approximated with GGX sampling of the reflected directions [WMLT07]. These assumptions allow modelling the material behaviour of rough non-conductive materials in the long-wave spectrum as presented in Yang and Buckius [YB95] for emission and as measured in Torrance and Sparrow [TS65] for reflections.

The first step for computing long-wave radiation consists in meshing the sky vault using the same kind of partition than for short-wave [BB14] but with 230 elements instead of 2400. Fewer elements are enough because the distribution of long-wave sky radiances is smoother than short-wave ones. Berdhal and Fromberg's clear sky model [BF82, EGA19] is used to estimate the anisotropic distribution of sky temperatures, based on measured air temperatures and relative humidity.

After this step, the net long-wave flux needs to be computed at each timestep for each element. The net flux is equal to the total emitted flux minus the total absorbed flux, hence the calculation is divided in two stages.

The total emitted flux is calculated at the barycentre of each element, which is an acceptable simplification if sufficiently fine meshes are used [CW93]. The flux is described as:

$$\phi_i^\varepsilon = \varepsilon_i^h \sigma T_i^4, \qquad (5)$$

where ε_i^h is the total hemispherical emissivity of element i, calculated by an integration of the directional emissivity of Figure 5 on the zenith angle.

The total absorbed flux is more complex to compute because it depends on the interaction of long-wave radiation with the scene. Since the geometry is permanent, a pre-computation of the inter-element relations that are exclusively geometry dependent is performed, in order to accelerate the simulation process. An absorption matrix, namely, $\mathbf{A}$, is pre-computed. $\mathbf{A}_{ij}$ contains a number between 0 and 1 that expresses the fraction of the black body radiant power of element j (σT_j^4) that is absorbed by element i. This number is difficult to obtain, because it depends on the directional absorptivity of i, and on the directional emissivity of j. Moreover, there is a fraction of this radiation that bounces on other elements before reaching i, and therefore the directional reflectivities of surrounding elements must be considered. Ray tracing is used to calculate $\mathbf{A}$, casting rays from the barycentre of each element, and considering non-diffuse absorptions, emissions and glossy reflections. The calculation of the direction of the reflected rays is presented in Section 3.2.2, because it is especially important in the rendering stage.

Once matrix $\mathbf{A}$ is pre-computed, the total absorbed radiation can be computed for every element multiplying the matrix by a vector of the black body radiant power of each element, based on its current temperature:

$$\phi_i^\alpha = \sum_{j=1}^{n} \mathbf{A}_{ij}(\sigma T_j^4). \qquad (6)$$

Combining Equations (5) and (6), the net radiative flux in the barycentre of element i is:

$$\phi_i = \phi_i^\varepsilon - \phi_i^\alpha = \sigma \left(\varepsilon_i^h T_i^4 - \sum_{j=1}^{n} A_{ij} T_j^4 \right). \qquad (7)$$

A non-linear solver is used in FEM to account for long-wave radiation, which means that several emitted and absorbed fluxes are calculated for each timestep of the simulation.
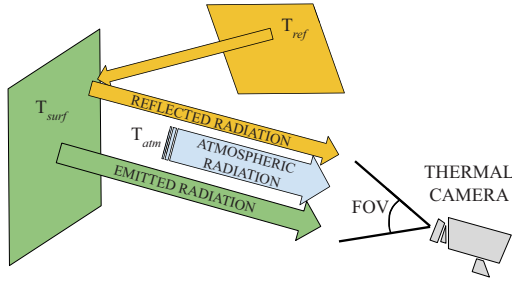
Figure 6: *Components of the radiation captured by a thermal camera.*

3.2. Thermography rendering

Once the surface temperatures are obtained, post-processing is needed to simulate the thermal camera. The final rendered thermograms are simulated by placing a virtual thermal camera inside the geometric model. This section describes the model used by real thermal cameras first, and then an algorithm for simulating the virtual camera is proposed.
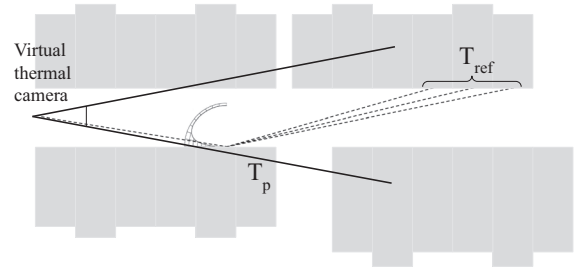
3.2.1. Thermal cameras

Thermal cameras are composed of a collection of infrared sensors that gather the incoming infrared radiative flux arriving in directions within the field of view (FOV) of the lens [VM17]. These sensors measure radiation with a wavelength between 7 and 14 μm, which is a mixture of three different components: radiation emitted by the captured object, radiation emitted by other bodies and reflected by the object and radiation emitted by the atmospheric layer between the camera and the object (Figure 6).

This simplified physical model is then used by the camera software to obtain an estimated temperature for each pixel. The model is based on the measured radiative flux and some data that must be entered to the camera: the emissivity ε, reflected temperature T_{ref}, air temperature and the relative humidity of the scene. The measured radiative flux is first used to estimate a total radiant power ϕ_{in}, following the spectral distribution of a black body. Then, the black body radiant power of the captured surface $\Phi^{black}(T_{surf})$ is estimated by subtracting the atmospheric and reflected components [VM17]:

$$\Phi^{black}(T_{surf}) = \frac{\phi_{in}}{\tau_{atm}\varepsilon} - \frac{1-\varepsilon}{\varepsilon}\Phi^{black}(T_{ref})$$
$$- \frac{1-\tau_{atm}}{\tau_{atm}\varepsilon}\Phi^{atm}(T_{atm}), \qquad (8)$$

where T_{surf} is the unknown surface temperature, and τ_{atm} is the atmospheric transmittance estimated using an atmospheric model with the input data. $\Phi^{atm}(T_{atm})$ is the radiant power of the atmosphere at temperature T_{atm}, output of the atmospheric model.

For a sufficiently short measurement distance, the atmospheric radiation can be neglected ($\tau_{atm} = 1$). Under these conditions, and taking into account that $\Phi^{black}(T_{surf})$ is equal to σT_{surf}^4 (Equation 1), the surface temperature is calculated using the following expression:

Figure 7: *Ray tracing for rendering a thermal image using a virtual camera.*

$$T_{surf} = \sqrt[4]{\frac{\phi_{in}}{\sigma\varepsilon} - \frac{1-\varepsilon}{\varepsilon}T_{ref}^4}. \qquad (9)$$

Moreover, if the input emissivity is set to be 1, the output temperatures are called *apparent surface temperatures* (T_{surf}^{app}). In this context, black body behaviour of materials is assumed, and the atmospheric radiation source is neglected:

$$T_{surf}^{app} = \sqrt[4]{\frac{\phi_{in}}{\sigma}}. \qquad (10)$$

3.2.2. Virtual thermal camera

The goal of thermography rendering is to imitate the image captured by a real camera, which does not show the real surface temperature of the scene but one estimated from the measured incoming radiation. In this sense, the most important calculation is the estimation of the virtual incoming radiative flux ϕ_{in}^{virt} for each pixel. In our study, this estimation is performed using the reverse of the real camera's approach (the reverse of Equation 9):

$$\phi_{in}^{virt} = \varepsilon\sigma T_p^4 + (1-\varepsilon)\sigma T_{ref}^4. \qquad (11)$$

The virtual flux ϕ_{in}^{virt} is computed based on the simulated temperature of the directly seen point (T_p), the reflected temperature (T_{ref}) and the corresponding pixel emissivity ε. The properties of the virtual camera must be set to be the same as the real thermal camera used in the measurement campaign (same FOV, pixel resolution, position and direction of view). The emissivity ε associated with each pixel is obtained using a directional emissivity model such as those described in Figure 5. Finally, the estimated temperature is calculated by replacing the computed ϕ_{in}^{virt} in Equation (10) to simulate the calculations done by the real thermal camera.

Ray tracing is used to obtain T_p and T_{ref}. For each primary ray, the temperature of the intersected point T_p is obtained and the reflected temperature is calculated as a weighted average of the temperatures of the points reached through the glossy reflected paths that follow the specular lobe. This process is graphically shown in Figure 7. Several primary rays are cast for each pixel to account for anti-aliasing. Reflections take a greater importance in the case where the angles of incidence are large, such as in the case of a small camera FOV and perspective views of the scene.

A micro-facet BRDF model [WMLT07] is used to compute the direction of reflected rays. The GGX probability density function is

Algorithm 1. Computation of virtual flux for each pixel

$C = \text{getCameraPosition}()$
for each pixel (u,v) **do**
    $dir = \text{getRayDirection}(u,v)$ ▷ get direction determined by the pixel
    $[i, p] = \text{castRay}(c,dir)$ ▷ returns intersected point p and element i
    $\varepsilon_i = \text{getDirectionalEmissivity}(i, \text{-}dir)$ ▷ Fig. 5
    $T_p = \text{getTemperature}(i,p)$ ▷ get temperature of directly seen point
    $\sigma T_{ref}^4 = 0$ ▷ initialize reflected flux
    for each reflected ray $r \in 1...L$ **do**
        $(reflDir, w_r) = \text{getGGXDirection}(i,dir)$ ▷ GGX weighted sampling
        $\sigma T_r^4 = \textsc{followSpecularPath}(p, reflDir)$
        $\sigma T_{ref}^4 \mathrel{+}= w_r * \sigma T_r^4 / L$
    end for
    $\phi_{in}^{virt}(u,v) = \varepsilon_i \sigma T_p^4 + (1-\varepsilon_i)\, \sigma T_{ref}^4$ ▷ Eq. 11
end for

---

function $\sigma T_r^4 = \textsc{followSpecularPath}(p, reflDir)$
    $rayCon = 1$
    $\sigma T_r^4 = 0$
    while $rayCon > t$ **do**   ▷ t is a threshold ≈ 0
        $[j, p] = \text{castRay}(p,reflDir)$
        $\varepsilon_j = \text{getDirectionalEmissivity}(j,\text{-}reflDir)$
        $\sigma T_r^4 \mathrel{+}= rayCon * \varepsilon_j * \sigma * \text{getTemperature}(j,p)^4$
        $reflDir = \text{getSpecularDirection}(j,reflDir)$
        $rayCon \mathrel{*}= 1 - \varepsilon_j$
    end while
end function

(a) Satelite view.   (b) Overall geometry.   (c) Mesh detail.

Figure 8: *Photo and model of Rue des Tonneliers, Bayonne, France. Satellite view extracted from Google Maps on 31 July 2019.*

4. Case of Study

The proposed simulation method was evaluated on a real case study, which was *Tonelliers* street in the city of Bayonne, France (Figure 8a). The selected environment is characterized by a high complexity from both a material and geometrical point of view. A highly detailed 3D model was developed (Section 4.1) taking into account the requirements for an FEM simulation, as described in Acuña *et al*. [APyMLLB18]. The simulations were compared with measured data retrieved from the urban thermographic campaign [GN19] summarized in Section 4.2.

4.1. 3D geometry

The urban model used for the simulations corresponds to an urban tissue mostly composed of eighteenth-century buildings. The preponderant construction technique in this urban area is a timber-framed system over a ground floor built of stone masonry. Wood, mortar and stone are therefore the predominant materials in the scene, although some other materials such as asphalt and glass windows are also present. The geometric modelling of this scene was based on an *in situ* survey by means of drones and light detection and ranging (LIDAR) techniques; the model was manually built using computer aided design tools. A high level of geometrical detail was used, which was important in the validation of the results with measured thermograms. The walls and inner floors were modelled with a constant thickness, which was set to 0.18 m following the average value obtained from *in situ* inspections.

The FEM simulations required a specific geometric modelling strategy called conformal meshing [ZTZ13]. A conformal mesh is one in which no node of an element is on an edge or face of another element, so that all adjacent elements share full edges. Regular hexahedrons and a small number of triangular prisms were used. The skin of the model, which is the part of the geometry subject to convective and radiative boundary conditions, is then composed of quadrilateral and triangular elements. The final model (Figure 8b) is meshed with 192 911 volume elements and 104 377 surface elements.

Building parts were modelled seeking for constructive realism. For example, wood and mortar elements together form the typical timber frame constructions that are present in Bayonne. Some windows were modelled with glass (if wooden blinds were opened during the campaign) and the rest of them with wood.
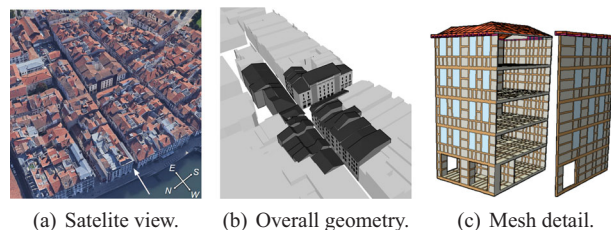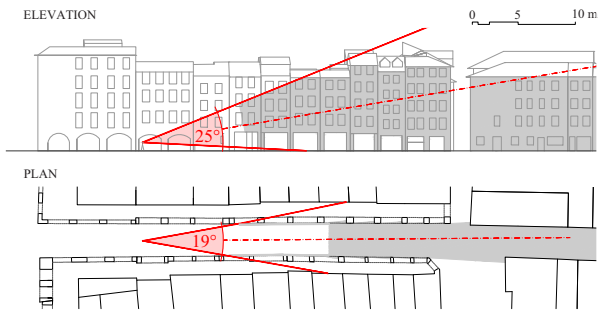
applied for sampling the specular lobe. This function is controlled by a unique roughness parameter α_g, which typically takes values between 0 and 1 [BS12]. Values closer to 0 indicate more specular reflections. A different α_g value is set for each material depending on its surface roughness. Following [WMLT07], an importance sampling strategy is adopted and different weights are assigned to each scattered direction. Hammersley low-discrepancy sequence [Suf16] is used to avoid noise in the final results. In contrast with [WMLT07], a unique reflectivity value that corresponds to the macrosurface normal is used for each primary ray, because the proposed emissivity curves already consider roughness.

Algorithm 1 presents a pseudocode that describes the computation of the virtual flux for each pixel. A ray is cast from the camera through the pixel and the temperature of the directly seen point is obtained using the results of the FEM processing stage. Next, L rays are cast to sample the reflected directions. Each reflected direction generates a different path (using followSpecularPath procedure) to obtain the temperature of the reflected elements using multiple radiation bounces. After the glossy sampling, the paths are built over the simplification of perfectly specular reflections, allowing for reasonable computational performance without producing a significant absolute error in the calculations.

Under clear sky conditions, the atmospheric transmissivity is high in the spectral range of the camera, because of the atmospheric window [Kru15]. This fact leads to an underestimation of the apparent sky temperature captured in thermography, which is affected by the much colder space background. In urban thermograms, the built surfaces can reflect the sky radiation. Hence, a new sky model, different to the one used in FEM, must be included in the rendering stage to reproduce the effect of the atmospheric window on the rendered thermograms. The model described by Bliss [BJ61] is used in this study.

Figure 9: *Position and view of the thermal camera in the measurement campaign.*

4.2. Measurement campaign and parameter set-up

The results from a measurement campaign were used to validate the simulations. The campaign was carried out on April 23 (spring), a day with clear sky and calm wind conditions. A thermal camera (FLIR B200, 240 × 180 pixels, FOV: 25º ×19º) was placed on the *Tonneliers* street, and a series of thermograms were taken during a period of 18 h (6 a.m. to 12 p.m.). The camera was set to capture the apparent surface temperature: the emissivity was set to 1 and the distance to 0 m.

Figure 9 shows the position of the camera and the surface captured by the camera lens. A perspective view of the scene was selected in order to acquire a maximal amount of physical information in a single frame. An example of photograph and correspondent thermogram can be observed in Figure 1.

Other environmental conditions were measured to estimate the correct boundary conditions in the simulations. The wind velocity was captured by an anemometer placed at 2.5 m from the ground. Street air temperatures and relative humidity were measured *in situ* (see Figure 10). A weather station located at 3.4 km away from the location provided the global horizontal irradiances. Short-wave reflectivities of the materials in the street (wood, mortar, stone, asphalt, roof tiles and glass) were estimated by measuring the luminance differences between each material and a baseline tape with a known reflectance, under the same lighting conditions. Finally, Meteonorm [RMKS10] data were used to define the ground temperature 1 m in depth, which was estimated to be 11.1 ºC, and constant for the period of measurement.
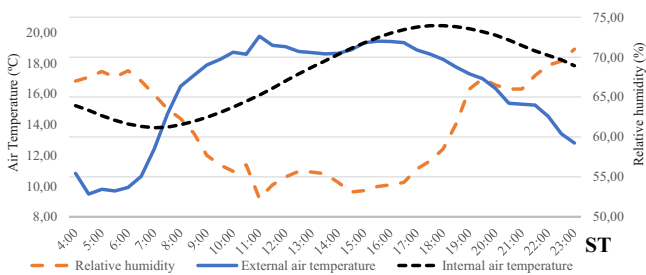
Figure 10: *Measured outside air temperature and relative humidity, along with the estimated internal air temperature.*

Table 1: *Parameter set-up for material properties.*

Material	k	ρ_m	c_p	r
Mortar	1.05	1400	1500	0.53
Wood	0.21	800	1255	0.45
Stone	3.50	2750	880	0.49
Asphalt	1.48	2267	1035	0.41
Roof tile	0.49	394	937	0.48
Glass	0.95	2500	836	0.1

Table 2: *Emissivity parameters for different materials, along with the GGX roughness parameter α_g.*

Material	$\varepsilon_\perp$	Fresnel	Diffuse	α_g
Mortar	0.91	15%	85%	0.28
Wood	0.95	10%	90%	0.40
Stone	0.96	30%	70%	0.14
Asphalt	0.92	20%	80%	0.21
Roof tile	0.90	50%	50%	0.05
Glass	0.92	100%	0%	0.00

The parameter set-up is shown in Table 1. The values for the conductivity components (k, ρ and c_p) were extracted from a reference material database [CST12], while short-wave reflectivity values r were averaged for each material.

Finally, the convective coefficient of the outside surfaces was set to $h = 10$ W m^{-2} K^{-1}, based on the low wind values that were measured *in situ* (lower than 1 m s^{-1}). For inside surfaces, the values extracted from the French thermal regulation [CST12] were the following: 0.7 W m^{-2} K^{-1} for the ground, 2.5 W m^{-2} K^{-1} for vertical walls and 5 W m^{-2} K^{-1} for roofs.

4.3. Emissivity estimations

The emissivity of urban surfaces plays a key role on the physically based simulation and rendering process. Measured directional emissivity models for urban materials are not available in the literature. In this work, following the process described in Figure 5, the directional emissivities were estimated using combination of ideal Fresnel and diffuse models. This assumption is based on *in situ* observations of material roughness, as well as on a second measurement campaign in the same street [BGN19], where two thermal cameras were used (the first one with a perspective view and the second one with a frontal view).

Table 2 shows the parameters chosen for the generation of directional emissivity curves. The Fresnel and diffuse percentages were estimated from the observations, and the normal emissivity values $\varepsilon_\perp$ were extracted from [FS06].

5. Implementation

The surface temperatures were simulated using the Cast3m code [CDP11] as the base FEM engine. A total of 24 h was simulated (midnight to midnight) with a timestep of 10 min (144 steps). Linear

shape functions were used. The input outside air temperatures used were those presented in Figure 10, which also presents the internal air temperatures that were obtained in the FEM simulation. The initial temperature conditions were obtained using a steady-state simulation for the first hour (00:00) under the imposed boundary conditions that were described above.

The Embree high performance ray tracing kernels [WWB*14] was used to accelerate the ray tracing modules (calculation of matrix **A** from Equation 6 and the rendering stage described in Algorithm 1). Different values of α_g were adopted depending on the material roughness in GGX sampling. The values for α_g are presented in Table 2. The number of reflected rays was set to be $L = 100$, and the threshold was $t = 10^{-5}$. Note that matrix **A** is an $n \times n$ matrix of floating point numbers, with $n \approx 100$ k. Following [AFB18], sparse representations were used to reduce the memory requirements of such matrix, leading to a total consumption of around 8 GB. Then, the non-diffuse long-wave radiation boundary conditions were implemented in Cast3m using the pre-computed matrix **A**. In the rendering stage, a window of 4×4 rays were cast for estimating the temperature of each pixel, in order to avoid aliasing in the rendered thermogram.

6. Results and Discussion

This section presents the result of the simulations and a comparison with the measured thermograms. All tests were executed on an Intel i7-7700 processor with four cores and 16 GB of RAM. In the pre-processing stage, the computation of short-wave loads took around 7 min, while the extended view factors matrix **A** using Embree took 11 min. FEM simulation (Cast3m) had the longest execution time, which was 62 min. With these results, post-processing took less than 10 s to render each thermogram.

The first results are shown in Figure 11 and correspond to the surface temperatures obtained with the FEM simulation. The results
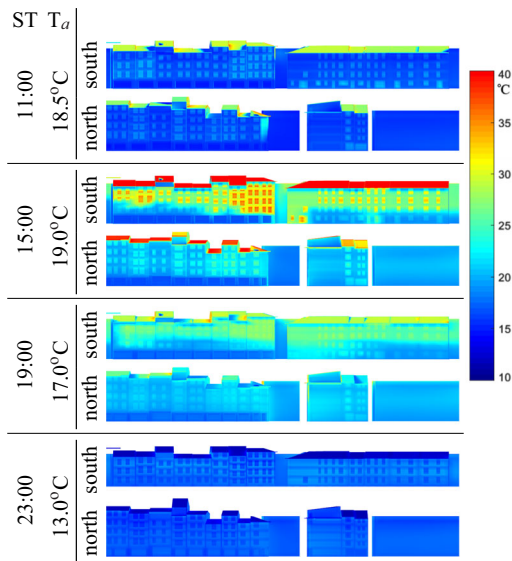
Figure 11: *Surface temperatures simulated with FEM. The results are separated into the north and south facing walls.*
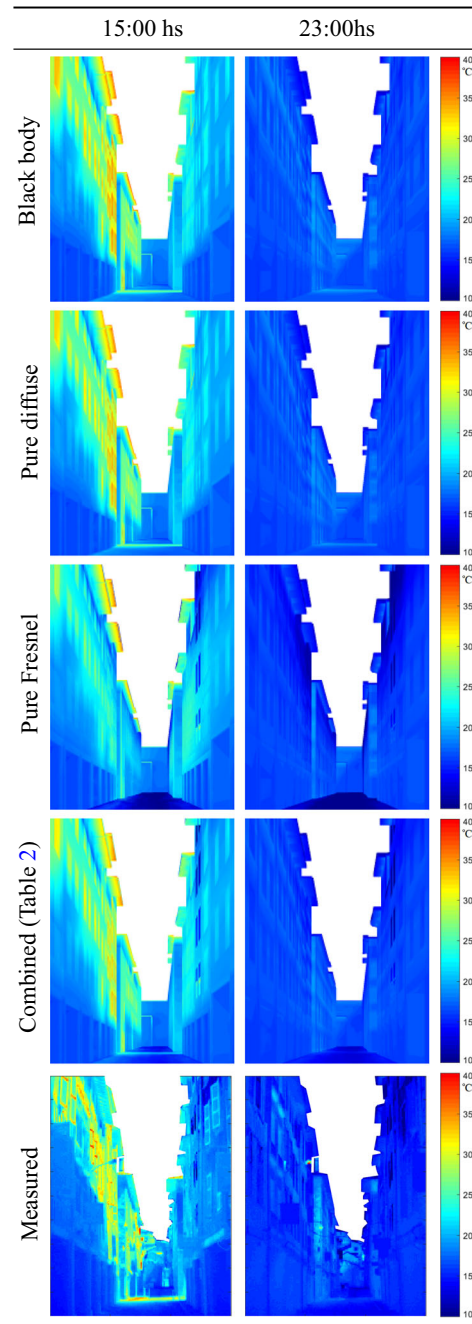
Figure 12: *Several rendered thermograms using different emissivity models along with measured results.*

are presented for the north and south street façades at four different times of the day. The results show cold surfaces in the morning (11:00 hours), mainly driven by the air temperatures. The surface temperatures begin to rise as the sunlight starts to impinge directly (15:00 hours). The thermal inertia of the walls keeps them hot during the evening (19:00 hours), while at night (23:00 hours) the simulation shows colder roof temperatures due to long-wave radiation
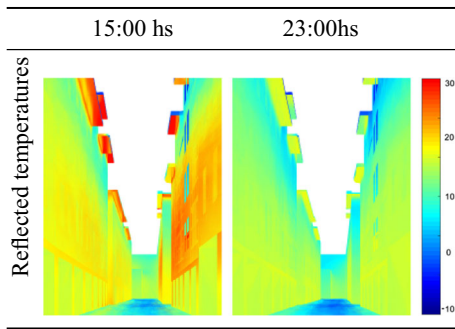
Figure 13: *Reflected temperatures of each pixel associated with the same camera position and two different hours. A new colour map interval is used to visualize the colder reflected temperatures of the sky.*

exchanges with the sky. This behaviour agrees with the one expected for an urban scene during a windless sunny day.

6.1. Impact of directional emissivity

In the urban test case considered, the inclusion of directional properties of infrared radiation did not pose a significant impact on the FEM temperature results. The absolute differences between using black body behaviour and mixed directional emissivities (Figure 5) was less than 1 °C for 99.9% of the exterior surfaces throughout the entire simulation period, with a mean difference of 0.1 °C and a standard deviation of 0.2 °C. However, in the rendering stage, directional emissivity plays a major role, and therefore we focus on studying its effect on the rendered thermograms.

For the next experiment, the virtual thermal camera was placed in the same position as in the measurement campaign. Two hours of the day were selected, one during daylight hours (15:00 hours) and the second one at night (23:00 hours). Thermal images were rendered using different directional emissivity models, in order to show the effect of this parameter on the results. Figure 12 depicts the rendering results (rows 1–4) and corresponding thermograms from the measurement campaign (last row).

The first row was generated using a black body model ($\varepsilon = 1$). Under this assumption, the wooden blinds on the south wall present higher temperatures than in the measurements, as well as the entire surface of the north facing wall.

When the emissitivity is set below 1 (as done in rows 2–4), the radiation reflections start having an effect on the results. Hence, to help the analysis, the glossy reflected temperatures captured by the virtual camera are shown in Figure 13, obtained by following the glossy reflected paths as described in Section 3.2. Two different colour map intervals were used for a better visualization of the reflected sky temperatures, which are much colder than the urban surfaces.

The results are more similar to the measurements when using a diffuse emission approximation (row 2 of Figure 12), where the surfaces are considered grey-body emitters. Here, the normal
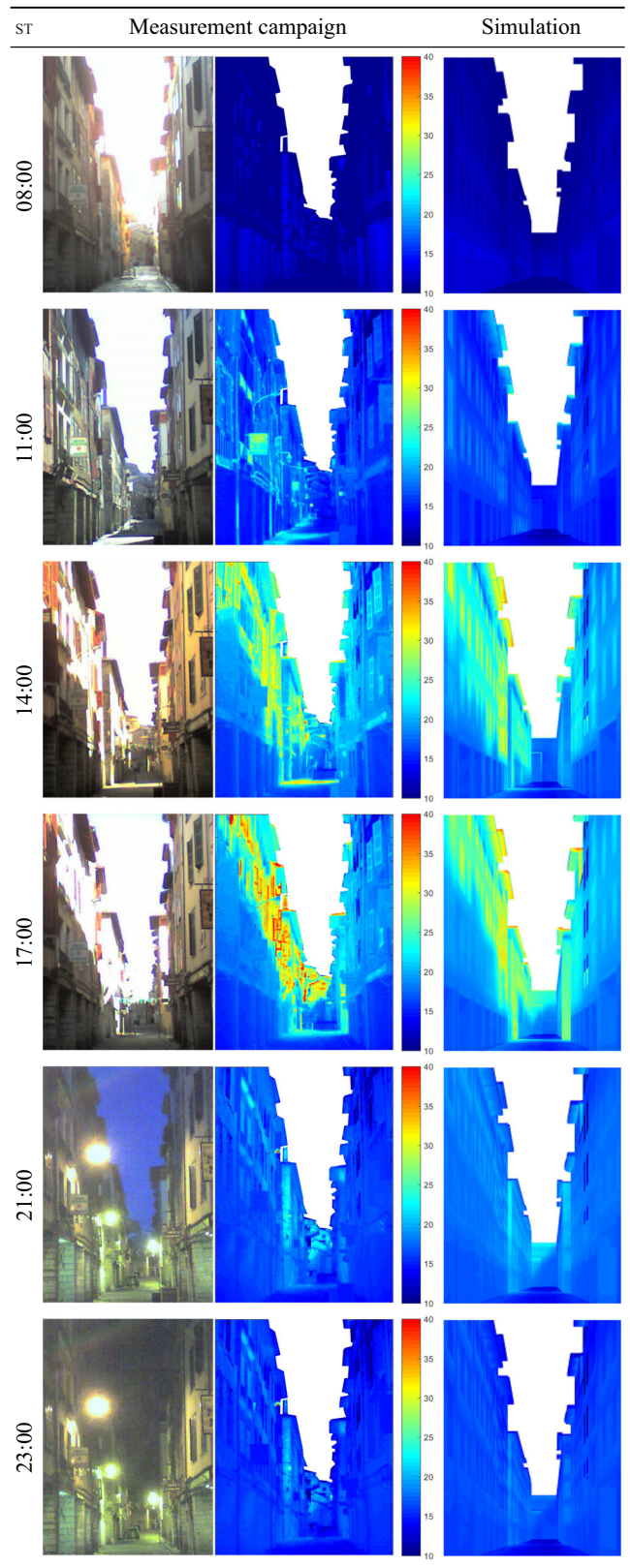
Figure 14: *Set of photographs, thermograms, and the simulated results between 08:00 and 23:00, Solar Time (ST)*

emissivity ($\varepsilon_\perp$) values from Table 2 were used as the constant emissivity for each material. In this case, the colder reflected temperatures of the sky start having an effect in the results, allowing for better results in the south wall, but non-rough surfaces (e.g. glass windows in the north wall) still present an overestimated emissivity. The third row was generated using the Fresnel emissivity model (Figure 2). In this case, the reflected temperatures have a major effect in the rendered images, which are much colder than in the measurements. These images are especially influenced by the large incidence angles of the perspective view, resulting in lower emissivity values. The images in the fourth row were generated using the mix of diffuse and Fresnel emissivity models with the percentages presented in Table 2. This model allows for the simulation of both smooth surfaces and diffuse ones: the wooden blinds show colder temperatures as in the third row, and the glass on windows reflect the sky temperatures. Upon comparison with the measurement results, the combined model proved to be the most accurate one. Therefore, this model was used in the rest of the analysis.

6.2. Time sequence of measured and rendered thermograms

The time-lapse of measured and simulated results is presented in Figure 14.

Thermal images are shown with the same colour map to facilitate the comparison. Temperature patterns are very similar between both set of images. During the day, the short-wave shadowing pattern drives the temperature distribution on the south walls, which is also observed in the simulations. Direct sunlight strikes these walls more perpendicularly around noon, resulting in a temperature rise. After 14:00 hours, the temperature of some elements that were not considered in the simulations (e.g. opened wooden blinds) rises. These elements, which have low reflectance and thermal inertia, produce higher maximal temperatures in the real thermogram than in the simulation (see the results for 17:00 hours).

After the sunset (around 20:00), surface temperatures are very dependent on the SVF, resulting in colder temperatures for surfaces that see bigger portions of the sky. This phenomenon is due to the key role of radiative cooling of surfaces towards the sky. The simulations show some differences in ground temperatures, probably due to an estimation bias in the sky temperatures or short-wave reflectivity. Both measurements and simulations show that the roof overhangs reduce the effect of long-wave cooling, resulting in higher temperatures in the top parts of walls.

In order to get a better visualization of the results and to analyse the differences between measurement campaign and simulations, two thermograms were studied with greater detail: one at daytime (14:00), where short-wave fluxes were dominant, and the second one at night (23:00), where the influence of long-wave radiation is greater. Both images are shown in Figure 15, where three quadrants and two lines were selected in the measured images. The corresponding quadrants and lines were selected in the simulated thermograms, looking to cover the same area of the real images that can be slightly deformed by the lens.

The content of the quadrants was extracted and zoomed-in in Figure 16. In this table, Dx means quadrant x of daytime thermogram, while Ny means quadrant y of nighttime thermogram. D1 shows the

temperature patterns caused by short-wave shadowing. The roofs are hotter in the simulation because a single material (roof tile) was considered, while in reality they have multiple layers with different properties. Windows reflecting the cold sky are observed in D2, and similar temperature patterns can be seen in D3. The section of the street that receives direct sunlight is colder in the simulation. N1 and N2 show the effect of the long-wave cooling process of the buildings at night, where the parts protected by the roof overhangs are hotter. Finally, D3 details a section of the street and a wall which were heated by short-wave radiation throughout the day and remain warmer than the rest of the street due to thermal inertia.

The temperature plots for each pixel of the lines are shown in Figure 17, which also contains the mean and standard deviation of the absolute error between both plots. DV stands for daytime vertical, while NH means nighttime horizontal. The plots show that accurate temperature estimations were obtained for both daytime and nighttime thermogr-ams. The temperature profiles have similar behaviours, showing larger biases in sections where the geometrical differences between the real scene and the 3D model are greater. For instance, the first pixels of DV cover parts of the wooden blinds that were opened in the measurement campaign. This kind of detail was neglected in the 3D model, leading to a deviation in the temperature profiles. The overall mean of the absolute error reaches its maximum value of 1.12 °C in DH, which is expected because the horizontal line covers built surfaces with a wide geometrical variety.

7. Conclusion

A methodology for the simulation and rendering of urban thermography was presented, providing a set of accurate methods to account for the radiative boundary conditions that are involved in urban heat transfer studies. The methodology is based on a combination of FEM to discretize the heat conduction differential equations, and ray tracing to address the radiation modules.

The comparison of simulated and measured data shows that very accurate results were obtained by the proposed algorithms. The computational model showed good performance, allowing for the analysis of results under different parameter configurations. The use of directional emissivities was necessary in the rendering stage, because the measured results were affected by the large incidence angles of perspective views.

The new methodology was developed as an incremental improvement over previous works [BGN19, ANGN*19]. These previous works were based on a simplified geometry of the scene, whereas in this paper, a higher level of detail geometry was integrated into the FEM solver. This approach enabled to obtain greater precision in the results upon comparison with the measured data. Modelling different building elements such as windows and roof overhangs, as well as using a wider material variety, proved to have an important effect on the short- and long-wave behaviour of the urban scene. Moreover, the addition of a post-processing stage to simulate the thermal camera allows for introducing physical aspects that were not considered in previous works.

Urban thermography rendering can be of fundamental help in the interpretation of a time sequence of thermal images. For example, the simulation results showed the significant influence of the low
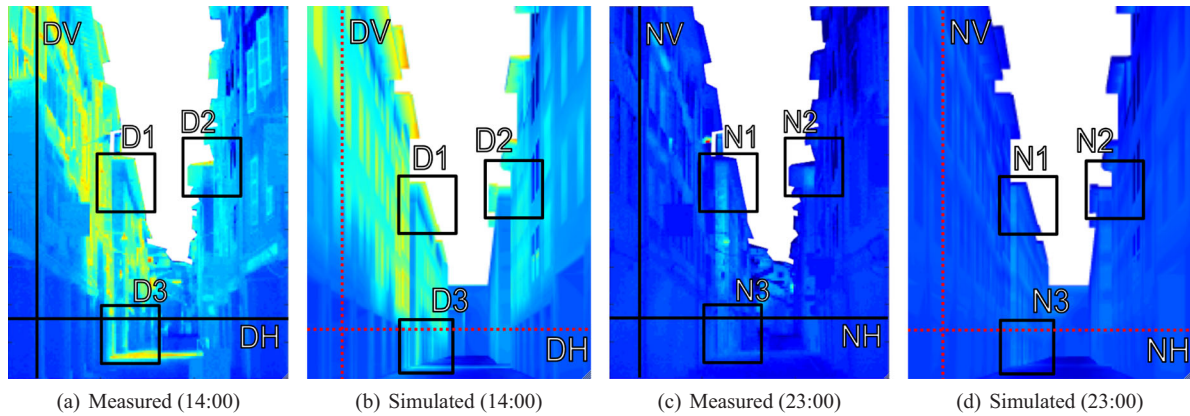
(a) Measured (14:00)   (b) Simulated (14:00)   (c) Measured (23:00)   (d) Simulated (23:00)

Figure 15: *Two measured and two simulated thermograms. For each image, three quadrants were selected and zoomed-in, and two lines of pixels were plotted.*
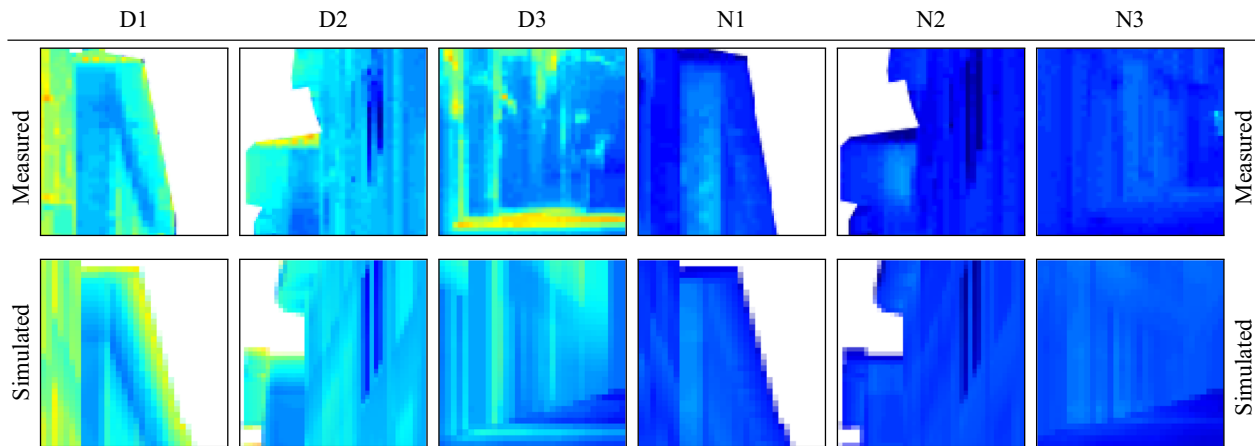

Figure 16: *Details of the measured and simulated thermograms.*

(a) DH, absolute error: μ=1.12ºC, σ_{dev}=1.10ºC

(b) NH, absolute error: μ=0.79ºC, σ_{dev}=0.66ºC

(c) DV, absolute error: μ=0.81ºC, σ_{dev}=0.91ºC

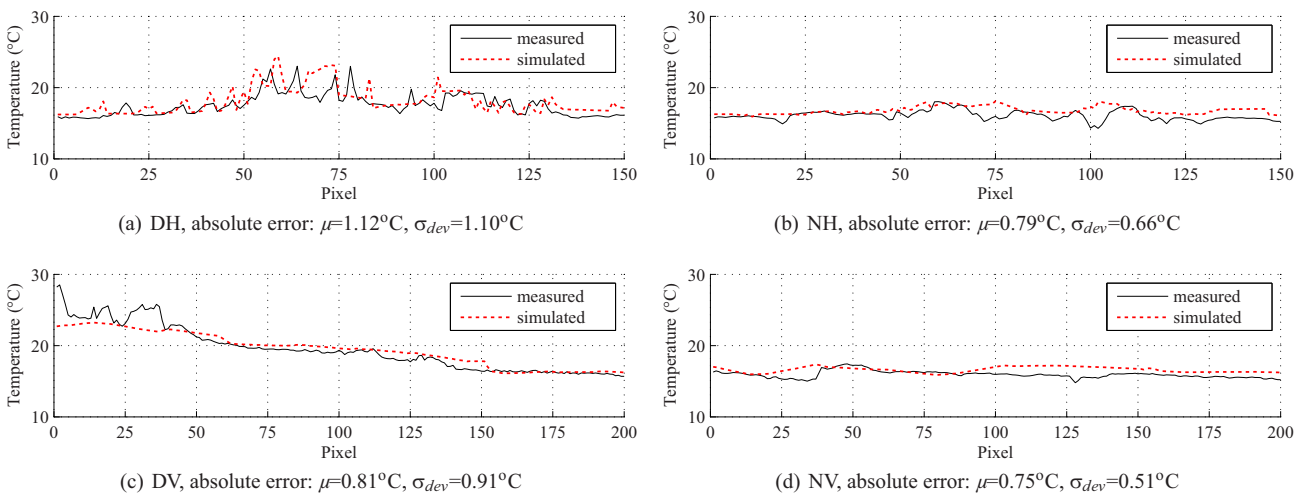(d) NV, absolute error: μ=0.75ºC, σ_{dev}=0.51ºC

Figure 17: *Temperature plots of horizontal and vertical lines of the selected thermograms.*

sky temperatures in the urban apparent surface temperatures. In this context, thermography rendering appears as an interesting tool to understand the main physical phenomenon that occurs in the urban landscape.

The graphical approach adopted in this study, where a set of thermal images were compared in detail, pushed the limits of urban thermal simulation methods. The results showed that rendering complex urban scenes, involving both rough and smooth materials, requires a precise treatment of directional emissivities and the proper reflectivity functions. Computer graphics algorithms provide many solutions to treat these kind of behaviours, but these properties are still a matter of study for physics. Therefore, thermography rendering provides a promising future avenue in the collaboration between both communities.

Future works should consider more detailed descriptions of the directional emissivity and reflectivity behaviour at the infrared spectrum. Micro-facet theory has proven to be an accurate tool for simulating rough surfaces, but the particularities of long-wave radiation must be analysed more carefully to select the best fitting functions. Comparing the simulations with thermal images captured with higher resolution cameras can also pose new challenges regarding geometrical modelling and computational performance. Here, a more detailed model of the thermal camera should be analysed to account for other phenomena. Performing measurement campaigns on different climate conditions, such as cloudy skies and/or windy days, is also a next step to improve the methodology.

Acknowledgements

References

[AFB18] Aguerre J. P., Fernández E., Beckers B.: Importance-driven approach for reducing urban radiative exchange computations. *Building Simulation 12*, 2 (Nov. 2018), 231–246.

[Agu20] Aguerre J. P.: ThRend: Infrared rendering for thermography simulation, Accessed in May 2020. https://github.com/jpaguerre/ThRend.

[ANGN*19] Aguerre J. P., Nahon R., Garcia-Nevado E., La Borderie C., Fernández E., Beckers B.: A street in perspective: Thermography simulated by the finite element method. *Building and Environment 148* (2019), 225–239.

[APyMLLB18] Acuña Paz y Miño J., Lefort V., Lawrence C., Beckers B.: Maquette numérique d'une rue du vieux bayonne pour son étude thermique par éléments finis. *A la pointe du BIM: Ingénierie et architecture, enseignement et recherche 1* (2018), 103.

[BB14] Beckers B., Beckers P.: Sky vault partition for computing daylight availability and shortwave energy budget on an urban scale. *Lighting Research & Technology 46*, 6 (2014), 716–728.

[BF82] Berdahl P., Fromberg R.: The thermal radiance of clear skies. *Solar Energy 29*, 4 (1982), 299–314.

[BGN19] Beckers B., Garcia-Nevado E.: Urban planning enriched by its representations, from perspective to thermography. In *Sustainable Vernacular Architecture*, Sayigh A., (Ed.), Springer International Publishing, Switzerland AG (2019), pp. 165–180.

[BJ61] Bliss Jr R.: Atmospheric radiation near the surface of the ground: A summary for engineers. *Solar Energy 5*, 3 (1961), 103–120.

[BS12] Burley B., Studios W. D. A.: Physically-based shading at disney. In *ACM SIGGRAPH* (2012), vol. 2012, pp. 1–7.

[CDP11] Charras T., Di Paola F.: *Utiliser Cast3M: la procédure PASAPAS*. Tech. rep., Commissariat á lénergie atomique, 2011.

[COM18] COMSOL Inc.: Comsol multiphysics 5.4: Heat transfer module user's guide, 2018.

[Cou06] Coulon N.: *Nouvel algorithme pour traiter le rayonnement thermique en milieu transparent dans CAST3M*. Tech. rep., Commissariat á l'énergie atomique, 2006.

[CST12] CSTB France C.: *Régles th-u – fasicule 4: Parois opaques*, 2012.

[CW93] Cohen M. F., Wallace J. R.: *Radiosity and Realistic Image Synthesis*. Academic Press, 1993. https://dblp.org/rec/books/daglib/0076870.bib.

[DICM05] Datcu S., Ibos L., Candau Y., Mattei S.: Improvement of building wall surface temperature measurements by infrared thermography. *Infrared Physics & Technology 46*, 6 (2005), 451–467.

[EDC14] Evins R., Dorer V., Carmeliet J.: Simulating external longwave radiation exchange for buildings. *Energy and Buildings 75* (2014), 472–482.

[EGA19] Evangelisti L., Guattari C., Asdrubali F.: On the sky temperature models and their influence on buildings energy performance: A critical review. *Energy and Buildings 183* (2019), 607–625.

[EGGA18] Evangelisti L., Guattari C., Gori P., Asdrubali F.: Assessment of equivalent thermal properties of multilayer building walls coupling simulations and experimental measurements. *Building and Environment 127* (2018), 77–85.

[FS06] Fronapfel E., Stolz B.: Emissivity measurements of common construction materials. In *InfraMation 2006 Proceedings* (2006), no. 12, FLIR Systems, ITC, pp. 212–220.

[GDAB*17] Garcia-Dorado I., Aliaga D., Bhalachandran S., Schmid P., Niyogi D.: Fast weather simulation for inverse procedural design of 3d urban models. *ACM Transactions on Graphics (TOG) 36*, 2 (2017), 21.

[GN19] García Nevado, E.,: *Termografía del cañón urbano: uso de la perspectiva para una evaluación térmica global de la calle*. PhD thesis, Universitat Politècnica de Catalunya, 2019.

[HB18] Haraké L., Burkard E.: Towards physically based material appearance in the thermal infrared spectrum: A short survey. In *Workshop on Material Appearance Modeling* (2018), Klein R., Rushmeier H., (Eds.), The Eurographics Association, pp. 37–40. https://doi.org/10.2312/mam.20181198.

[HMLV12] Hénon A., Mestayer P., Lagouarde J.-P., Voogt J.: An urban neighborhood temperature and energy study from the capitoul experiment with the solene model. *Theoretical and Applied Climatology 110*, 1–2 (2012), 177–196.

[HMS15] Howell J., Menguc P., Siegel R.: *Thermal Radiation Heat Transfer* (6th edition). CRC Press, Boca Raton, FL. Sept. 2015. https://doi.org/10.1201/b18835.

[KBBH19] Kottler B., Burkard E., Bulatov D., Haraké L.: Physically-based thermal simulation of large scenes for infrared imaging. In *Proceedings of the 14th International Joint Conference on Computer Vision, Imaging and Computer Graphics Theory and Applications* (2019), SCITEPRESS - Science and Technology Publications, pp. 53–64. https://doi.org/10.5220/0007351400530064.

[Kru15] Kruczek T.: Use of infrared camera in energy diagnostics of the objects placed in open air space in particular at non-isothermal sky. *Energy 91* (2015), 35–47.

[KSB*08] Kwan Y.-T., Sawtelle S., Bernstein U., Pereira W., Less D.: A simulation for hyperspectral thermal IR imaging sensors. In *Algorithms and Technologies for Multispectral, Hyperspectral, and Ultraspectral Imagery XIV* (Apr. 2008), Shen S. S., Lewis P. E., (Eds.), SPIE, pp. 65–75. https://doi.org/10.1117/12.777845.

[LBM*09] Li H., Bai T., Ma S., Lv X., Gao P., Yang W., Feng J.: An infrared imaging computation model and its validation. In *International Symposium on Photoelectronic Detection and Imaging 2009: Advances in Infrared Imaging and Applications* (July 2009), Puschell J., mei Gong H., Cai Y., Lu J., dong Fei J., (Eds.), SPIE, pp. 252–262. https://doi.org/10.1117/12.835063.

[LCDG07] Latger J., Cathala T., Douchin N., Goff A. L.: Simulation of active and passive infrared images using the SE-WORKBENCH. In *Infrared Imaging Systems: Design, Analysis, Modeling, and Testing XVIII* (Apr. 2007), Holst G. C., (Ed.), SPIE, pp. 35–45. URL: https://doi.org/10.1117/12.724822.

[LHK*10] Lagouarde J.-P., Henon A., Kurz B., Moreau P., Irvine M., Voogt J. A., Mestayer P. G.: Modelling daytime thermal infrared directional anisotropy over Toulouse city centre. *Remote Sensing of Environment 114*, 1 (2010), 87–105.

[LJ60] Liu B. Y., Jordan R. C.: The interrelationship and characteristic distribution of direct, diffuse and total solar radiation. *Solar Energy 4*, 3 (1960), 1–19.

[LNS04] Lewis R. W., Nithiarasu P., Seetharamu K. N.: *Fundamentals of the Finite Element Method for Heat and Fluid Flow*. West Sussex, England: John Wiley & Sons, 2004.

[LSF99] Li X., Strahler A. H., Friedl M. A.: A conceptual model for effective directional emissivity from nonisothermal surfaces. *IEEE Transactions on Geoscience and Remote Sensing 37*, 5 (1999), 2508–2517.

[MBP18] Muñoz D., Besuievsky G., Patow G.: A procedural approach for thermal visualization on buildings. In *Proceedings of the XXVIII Spanish Computer Graphics Conference* (2018), Eurographics Association, pp. 109–117.

[MGG*10] Maréchal N., Guérin E., Galin E., Mérillou S., Mérillou N.: Heat transfer simulation for modeling realistic winter sceneries. *Computer Graphics Forum 29*, 2 (May 2010), 449–458. https://doi.org/10.1111/j.1467-8659.2009.01614.x.

[Mod03] Modest M.: *Radiative Heat Transfer*. Elsevier, 2003. https://doi.org/10.1016/b978-0-12-503163-9.x5000-0.

[NGDA*16] Nishida G., Garcia-Dorado I., Aliaga D. G., Benes B., Bousseau A.: Interactive sketching of urban procedural models. *ACM Transactions on Graphics (TOG) 35*, 4 (2016), 130.

[PJH16] Pharr M., Jakob W., Humphreys G.: *Physically Based Rendering: From Theory to Implementation*. Cambridge, MA, USA: Morgan Kaufmann, 2016.

[PMMR*06] Poglio T., Mathieu-Marni S., Ranchin T., Savaria E., Wald L.: Osiris: a physically based simulation tool to improve training in thermal infrared remote sensing over urban areas at high spatial resolution. *Remote Sensing of Environment 104*, 2 (2006), 238–246.

[PRS16] Peeters J., Ribbens B., Steenackers G.: Determining directional emissivity: Numerical estimation and experimental validation by using infrared thermography. *Infrared Physics & Technology 77* (2016), 344–350.

[PSM93] Perez R., Seals R., Michalsky J.: All-weather model for sky luminance distribution–preliminary configuration and validation. *Solar Energy 50*, 3 (1993), 235–245.

[RGMB18] Rodler A., Guernouti S., Musy M., Bouyer J.: Thermal behaviour of a building in its environment: Modelling, experimentation, and comparison. *Energy and Buildings 168* (2018), 19–34.

[RMKS10] Remund J., Mueller S., Kunz S., Schilter C.: *Meteonorm handbook part I: Software*. Tech. rep., Switzerland, Tech. Rep, 2010.

[Sch94] SCHLICK C.: An inexpensive brdf model for physically-based rendering. *Computer Graphics Forum 13*, 3 (1994), 233–246.

[SNY18] STOLARSKI T., NAKASONE Y., YOSHIMOTO S.: *Engineering Analysis With ANSYS Software*. Kidlington, Oxford, UK: Butterworth-Heinemann, 2018.

[SP89] SILLION F., PUECH C.: A general two-pass method integrating specular and diffuse reflection. In *ACM SIGGRAPH Computer Graphics* (1989), vol. *23*, ACM, pp. 335–344.

[Suf16] SUFFERN K.: *Ray Tracing From the Ground up*. Wellesley, MA, USA: AK Peters/CRC Press, 2016.

[SW98] SNYDER W., WAN Z.: Brdf models to predict spectral reflectance and emissivity in the thermal infrared. *IEEE Transactions on Geoscience and Remote Sensing 36*, 1 (1998), 214–225.

[SWZF97] SNYDER W., WAN Z., ZHANG Y., FENG Y.-Z.: Thermal infrared (3–14 μm) bidirectional reflectance measurements of sands and soils. *Remote Sensing of Environment 60*, 1 (1997), 101–109.

[THC*19] TSESMELIS T., HASAN I., CRISTANI M., GALASSO F., DEL BUE A.: Rgbd2lux: Dense light intensity estimation with an FGBD sensor. In *2019 IEEE Winter Conference on Applications of Computer Vision (WACV)* (2019), IEEE, pp. 501–510.

[TS65] TORRANCE K. E., SPARROW E. M.: Biangular reflectance of an electric nonconductor as a function of wavelength and surface roughness. *Journal of Heat Transfer 87*, 2 (1965), 283–292.

[vE13] VAN EEKELEN T.: Radiation modeling using the finite element method. *Solar Energy at Urban Scale* (2013), 237–257.

[VM17] VOLLMER M., MÖLLMANN K.-P.: *Infrared Thermal Imaging: Fundamentals, Research and Applications*. Weinheim, Germany: John Wiley & Sons, 2017.

[War94] WARD G.: The RADIANCE lighting simulation and rendering system. In *Proceedings of the 21st Annual Conference on Computer Graphics and Interactive Techniques* (New York, NY, USA, 1994), SIGGRAPH '94, ACM, pp. 459–472.

[WMLT07] WALTER B., MARSCHNER S. R., LI H., TORRANCE K. E.: Microfacet models for refraction through rough surfaces. *Rendering Techniques* (2007). http://diglib.eg.org/handle/10.2312/EGWR.EGSR07.195-206.

[WWB*14] WALD I., WOOP S., BENTHIN C., JOHNSON G. S., ERNST M.: Embree: a kernel framework for efficient CPU ray tracing. *ACM Transactions on Graphics (TOG) 33*, 4 (2014), 143.

[WZCH15] WU X., ZHANG J., CHEN Y., HUANG X.: Real-time mid-wavelength infrared scene rendering with a feasible BRDF model. *Infrared Physics & Technology 68* (2015), 124–133.

[YB95] YANG Y., BUCKIUS R. O.: Surface length scale contributions to the directional and hemispherical emissivity and reflectivity. *Journal of Thermophysics and Heat Transfer 9*, 4 (1995), 653–659.

[ZTZ13] ZIENKIEWICZ O., TAYLOR R., ZHU J.: *The Finite Element Method: Its Basis and Fundamentals* (7th edition). Kidlington, Oxford, UK: Elsevier, 2013.